THE PENNSYLVANIA STATE UNIVERSITY
SCHREYER HONORS COLLEGE

DEPARTMENT OF ELECTRICAL ENGINEERING

SURFACE METHODOLOGY FOR 3D PRINTED MULTISPECTRAL SYSTEMS

JOSHUA C DAVIDSON
SPRING 2019

A thesis
submitted in partial fulfillment
of the requirements
for a baccalaureate degree
in Electrical Engineering
with honors in Electrical Engineering

Reviewed and approved* by the following:

Timothy Joseph Kane
Professor of Electrical Engineering
Thesis Supervisor and Honors Advisor

Ram Mohan Narayanan
Professor of Electrical Engineering
Faculty Reader

* Signatures are on file in the Schreyer Honors College.

ABSTRACT

In this study, a methodology is developed to enhance additively manufactured surfaces for use as 3D printed optical mirrors. Utilizing vacuum deposition and pulse-reverse-current electroplating, a grain size smaller than one-tenth the wavelength can be achieved for mmWave, IR, visible, and UV. A shared-aperture, multispectral imaging system consisting of 3D printed optical mirrors is proposed for military and security applications. Being centered and aligned along the same optical axis provides the advantage of exploiting multi-beam target illumination while maintaining a consistent reference for image processing. With the use of additive manufacturing and surface treatment techniques, complex designs can be achieved to develop passive apertures with predictable resolution and dimensional tolerance. Optimization and integration of this surface methodology would enable the ability to additively manufacture multispectral optical systems.

Keywords: Additive Manufacturing, IR, Infrared, Millimeter Wave, Imaging, Multimodal, Shared, Combined Aperture, Freeform optics, Gradient Index, GRIN, Pulse Electroplating

TABLE OF CONTENTS

LIST OF FIGURES

LIST OF TABLES

ACKNOWLEDGEMENTS

This work is supported by US Army Night Vision and Electronic Sensors Directorate (NVESD) Contract Number W909MY-12-D-0008 through MTEQ Purchase Order 27701. We appreciate technical discussions with Dr. Nibir Dhar of NVESD. We also thank our Penn State University colleagues, Andrew Fitzgerald for his expertise electroplating components and Dr. Bangzhi Liu for helping with FESEM imaging at the Nanofabrication Lab, Materials Research Institute. In addition, we thank Andrew O'Neill for providing the design of the 94 GHz horn antenna.

Chapter 1

Introduction

Integrating additive manufacturing into a world of imaging technology will introduce a degree of practicality in the complexity and design of multispectral systems. This investigative analysis reviews the performance of imaging applications for selected windows of electromagnetic radiation and discusses experimental results for additively manufactured optical components. Section 1 provides an overview of millimeter wave (mmWave), infrared (IR), and ultraviolet (UV) technology and applications. Section 2 is an outline of surface treatment methodologies with consideration of alternative methods. Section 3 includes experimental results and observations of surface characteristics for 3D printed optical mirrors. Section 4 is a discussion on novelty, demonstration, and topics for further development. Section 5 concludes this study with a brief summary.

1.1 Millimeter Wave Imaging

This section discusses the attenuation of mmWave signals due to scattering and absorption through various atmospheric conditions. Imaging applications are reviewed for frequencies from 30 to 300 GHz which are considered to fall within the mmWave region. A thorough historical review [1] on mmWave technology provides insight into the advancement of electronics, software, and imaging capabilities.

Attenuation of electromagnetic radiation from the scene to the detector is dependent on the signal's frequency and the media through which the signal travels. Figure 1 illustrates the unique performance of mmWave, infrared, and visible regions through media influenced by atmospheric conditions. Results show frequencies less than 100 GHz outperform higher frequencies during fog, drizzle, and rain. Similar results are observed for media consisting of particles less than the operating wavelength such as clouds, smoke, haze, dry snow, sand and dust.

There are notable differences in an experiment comparing the performance of imagers operating at 35 GHz, 94 GHz, and 140 GHz [2]. 94 GHz contains the best image resolution and contrast while 35 GHz provides the greatest range of temperature but does not offer good resolution. Yet, 35 GHz was the only frequency unperturbed by fog with cloudy skies. 140 GHz provides mediocre image quality, but it has the advantage of low power consumption. It also performs just as well with an 18-inch aperture as it does with a 12-inch aperture.

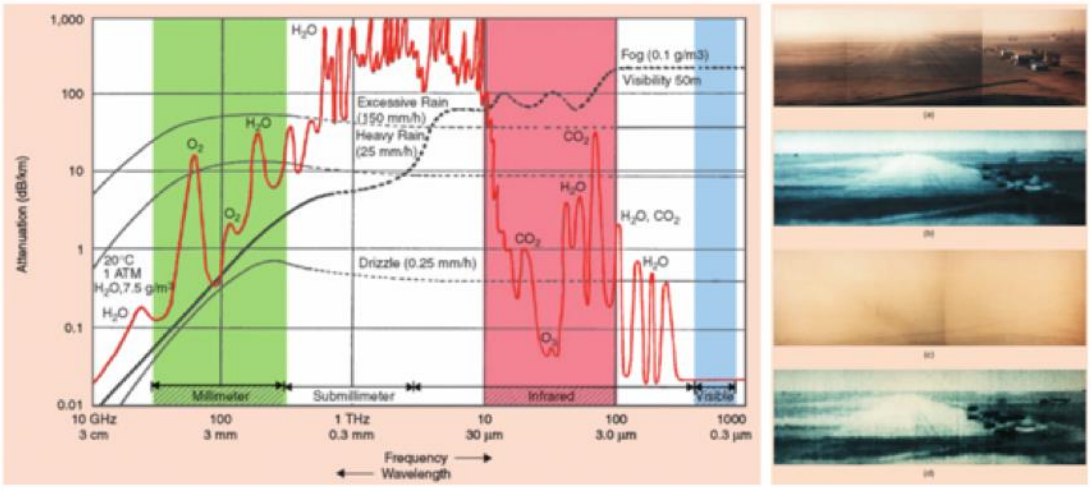

Figure 1: (LEFT) Attenuation of electromagnetic radiation during rain and fog, (RIGHT) (a) and (c) are visible images of a runway for clear and foggy weather, (b) and (d) are corresponding mmWave images at 94 GHz [3].

An extensive experiment performed over the sea in France provides information about the attenuation of polarized signals at 35 GHz and 94 GHz during rain, fog, and snow [4]. The study describes a relationship between particle dimensions and signal attenuation such that particle dimensions greater than the wavelength are more likely to scatter and attenuate the signal. For rainy conditions, results show less attenuation for vertical polarization than horizontal due to the wider horizontal dimension of rain drops. During fog, there is little attenuation for millimeter waves at 35 and 94 GHz since particle dimensions are less than the wavelength. During snow, results show little attenuation when the snow is dry but high attenuation when the snow is wet. In addition, another study performed in 2008 determined there is little attenuation at 95 GHz during dust storms [5] which can also be explained by considering particle dimensions.

A mmWave system operating at 93 GHz with a 2-foot aperture and a sensitivity of 0.3 K was tested for helicopter obstacles in a sandy environment [6]. The imager is capable of simultaneously measuring horizontal, vertical, and 45-degree polarizations of obstacles such as sand, cinder blocks, chain link fencing, a j-log, a wooden post, berms, and ditches. The study found different polarizations are better used for some obstacles than others by observing differences in their radiometric brightness. Therefore, specific frequencies and polarizations need to be selected to provide the most information about a given scene.

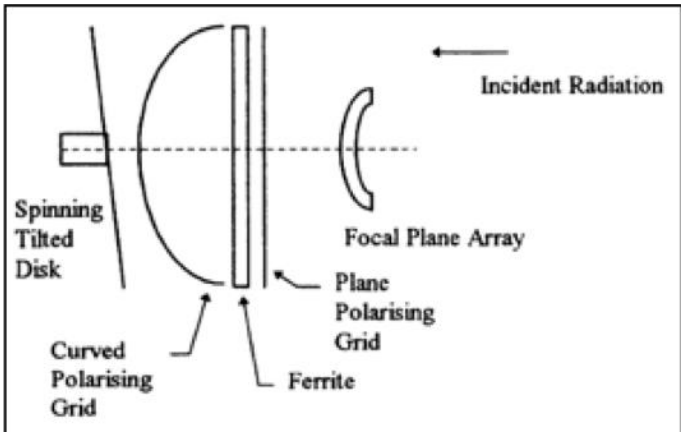

Figure 2: Optical schematic for passive mmWave imager [7].

An imager operating between 80 GHz to 105 GHz and capable of imaging multiple polarizations is designed for helicopter collision avoidance. It has an 80-degree by 40-degree field of view, a 30 cm diameter, a frame rate of 25 Hz, and a sensitivity of about 1-degree C [7]. The optical schematic is shown in Figure 2 which consists of a spinning tilted disk for scanning and a focal plane array of almost 100 channels. The optical system is very compact and is observed to have low optical aberrations.

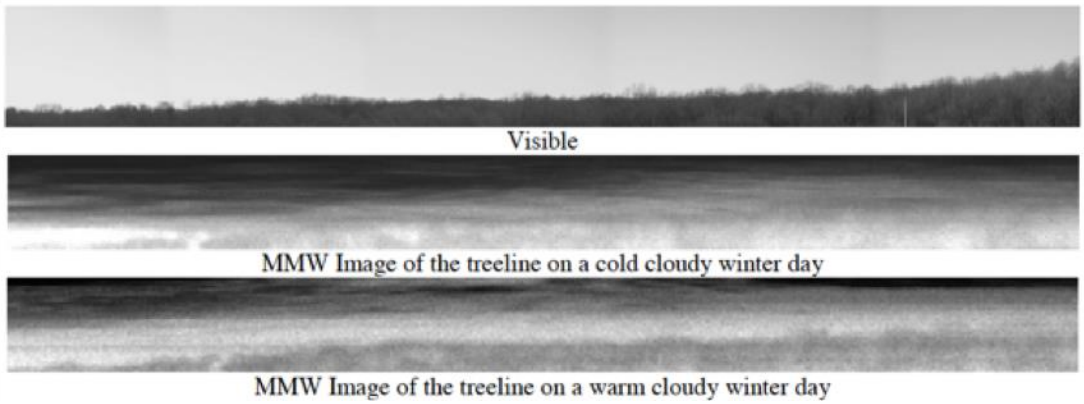

Figure 3: Comparison of visible images with mmWave images for tree lines [8].

In another experiment, data were collected to compare visible and mmWave images of tree lines and the tops of buildings for aircraft obstacle avoidance. The imaging system uses a 93-GHz Stokes-vector radiometer with a sensitivity of 0.4 K and a 2-foot parabolic antenna [8].

With a Stokes-vector radiometer [9], every polarization can be observed and analyzed. This provides a great amount of information that would otherwise be unexploited by most other radiometers. Figures 3 and 4 illustrate scenes that show how mmWave imagers perform under different conditions. Figure 3 depicts tree lines which show mmWave images during cold and warm winter days. While the mmWave images show contrast between the sky and trees, it is not as sharp as the visible image. Cold and warm days do not seem to make a significant difference for mmWave images. This insinuates similar results would be observed at night unlike visible imaging. Figure 4 depicts the top of a building which demonstrates mmWave images can be used to detect and differentiate buildings from the sky with good contrast and reasonable resolution. The image was taken during a clear, warm, sunny day where the concrete was exposed to warm temperatures before being imaged which explains the large contrast.

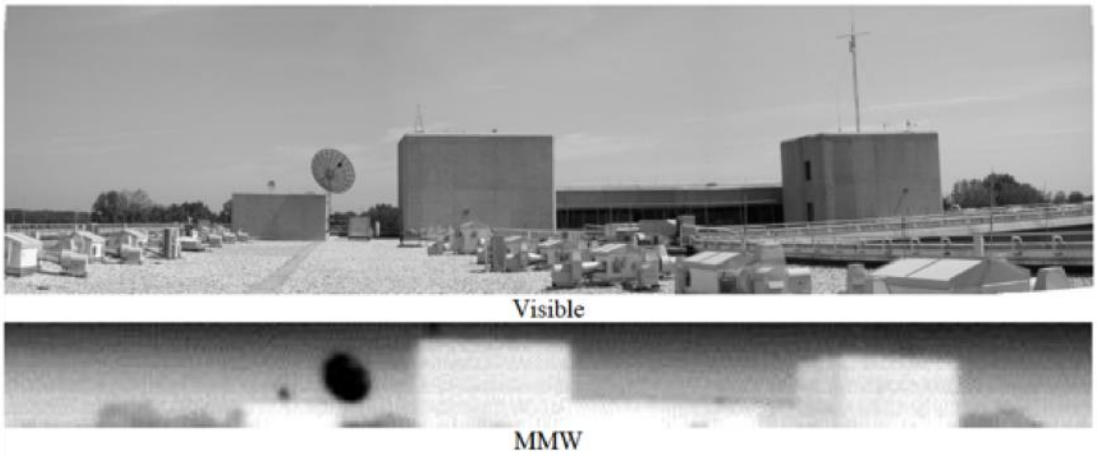

Figure 4: Comparison of visible images with mmWave images for the top of a building [8].

In summary, it is important to consider the atmospheric conditions through which mmWave signals will travel because the signals can be attenuated due to scattering and absorption. Millimeter waves can travel through clouds, fog, smoke, haze, sand and dust, dry snow and drizzle-like rain. However, wet snow or heavy rain cause greater attenuation because

the particle dimensions are larger than the operating wavelength. In addition, observing multiple polarizations with a device similar to a Stokes-vector radiometer can provide more valuable information than viewing only a single polarization. Altitude also has an impact because absorption contributes to the attenuation closer to ground level from higher concentrations of water vapor and molecular oxygen. There are several references available for information regarding radiometric remote sensing [10] and atmospheric attenuation [11, 12, 13, 14, 15].

1.2 Infrared Imaging

Infrared radiation is typically divided into the bands near (NIR), short wave (SWIR), midwave (MWIR), long wave (LWIR), and far (FIR). The entire infrared region spans wavelengths from deep red around 0.7 μm (~ 428 THz) to about 1000 μm (~ 300 GHz) which approaches the microwave and mmWave regimes. Infrared imaging is a form of radiometric measuring similar to mmWave imaging. However, it operates in a different window of the electromagnetic spectrum.

A simulation was conducted to analyze the atmospheric transmission of visible wavelengths around 0.4 μm (blue) to LWIR wavelengths around 9.4 μm [16]. In Figure 5, results show performance is dependent on temperature by illustrating the transmittance with respect to distance for each IR band during summer and winter seasons. During the summer season when temperatures are warm, SWIR outperforms the other bands and is observed at 5 km with 50% transmittance. On the other hand, during the winter season when temperatures are cold, LWIR outperforms the other bands and is observed at 6 km with 50% transmittance.

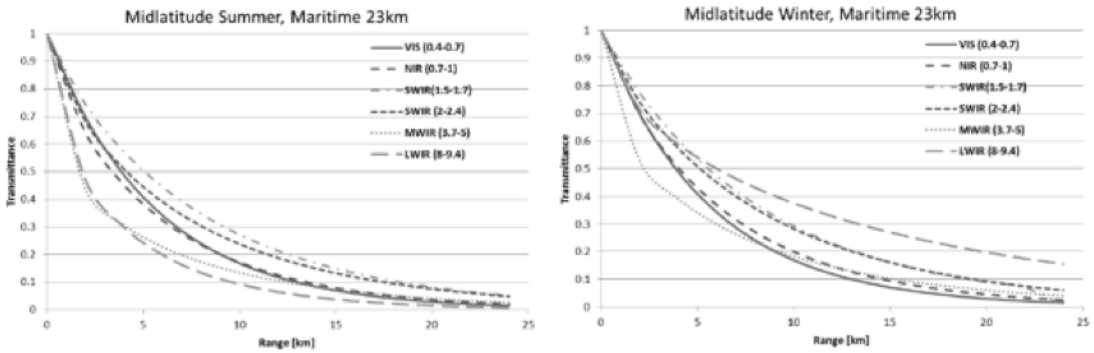

Figure 5: Transmittance for VIS, NIR, SWIR, MWIR and LWIR wavebands (spectral averaging) [16].

Table 1 contains data showing transmission trends for wavelengths 0.55 μm (green), 1 μm, 3.7 μm, and 10 μm through haze and different variations of fog [17]. For this situation, a haze is defined by meteorologists to have an observable optical density less than 2 per km for a wavelength of 0.55 μm. The data shows longer wavelengths transmit farther for every scenario. However, in a stable fog, there is much more attenuation than other variations of haze.

Table 1: Distance of perception in meters [17].

	Wavelength, microns			
	0.55	1	3.7	10
Haze, $d=2$/km	910	1820	5000	20 000
Small drops; very selective fog, $d=7.7$/km	260	370	1300	5000
Small drops; fog, $d=28$/km	71	80	107	189
Stable fog, $d=29$/km	68	68	67	125

A study comparing IR imagery and mmWave imagery suggests fusing the two together to provide covert passive imaging capabilities in dark situations and poor visibility for navigating hazards and detecting other features [18]. The study was conducted on an overcast, dry morning and indicates IR and mmWave imagers perform uniquely from one another due to differences in emissivity, illumination, resolution, and thermal sensitivity. The emissivity of a material varies with frequency and, therefore, does not appear the same for IR and mmWave devices. In fact, the

cooling of a hot object may reduce the IR signature whereas the mmWave signature would remain unaffected. Also, for mmWave imagers, there is a high contrast signature for metals. This is due to the dependence on radiometric temperatures being reflected from the surface which; for outdoor settings, it is typically a reflection of the cold sky as depicted in Figure 6. For comparison, most IR imagers have better resolution while most mmWave imagers have a wider field of view. In addition, most IR imagers have better thermal sensitivity than mmWave imagers but they can be similar under certain circumstances where there is good illumination of metallic objects.

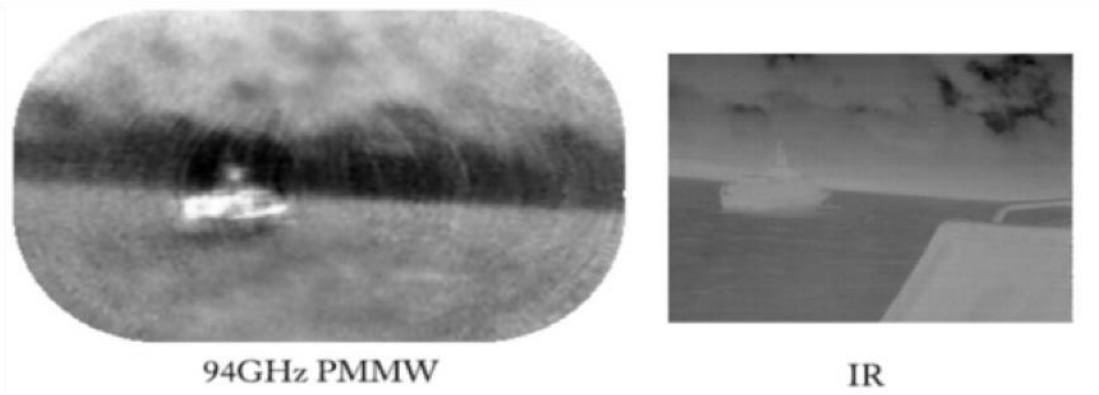

Figure 6: Comparison of mmWave and IR images of a moored boat [18].

For helicopter avoidance, an experiment implemented a 94-GHz Schmidt-Cassegrain antenna consisting of 5 rows of 30 receivers to detect overhead cable wires [19]. Results indicate passive mmWave imagery slightly outperforming longwave infrared imagery for detecting distant overhead cables as shown in Figure 7. The LWIR image may have better resolution but it cannot distinguish a cable from the surrounding sky. Whereas, the mmWave image has poor resolution but the cable can be identified.

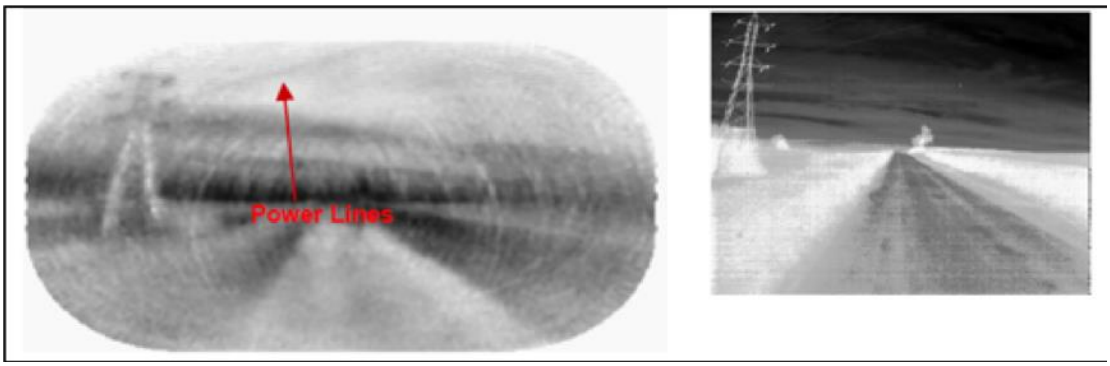

Figure 7: mmWave imagery (LEFT) and LWIR imagery (RIGHT) at night [19].

IR technology is widely used in the military field, medical field, power field, building field, agriculture and forestry, and the industrial field [20]. The military incorporates IR into missile guidance systems, IR night vision, and IR communication. IR thermal images are used in the medical field to visualize minute changes in a human's body heat for tumor detection or diagnosing lumbar disc. In the power field, thermal imagers are used to reliably prevent potential equipment failures due to thermal stress and overheating. For the building field, IR is used to test the tightness of air conditioning and ventilation ducts by mapping a temperature profile. In agriculture, IR is used for detecting and preventing certain plant diseases by searching for signatures of early signs. In the automotive industrial field, IR imagers are used as a safety features for back-up cameras and spatial sensors.

Additionally, IR imaging is used for buried landmine detection [21, 22]. A simulation correctly identified landmines beneath soil to a depth of 1 cm, but the detection began to fail for landmines deeper than 1 cm. Also, IR signals are typically sent through optical fiber systems and used for free space optical (FSO) communication [23].

In summary, IR signals are capable of traveling long distances through free space with little attenuation compared to the mmWave band. SWIR performs best during warm

temperatures and LWIR performs best during cold temperatures. Although IR may travel through a haze, the signal is strongly attenuated through any forms of fog. When compared to mmWave imagers, IR imagers have better resolution and thermal sensitivity but the contrast of target signatures can vary depending on the temperatures and illumination of the target and surroundings. Together, IR and mmWave technology can maximize imaging capabilities and reduce the inherent limitations of their respective frequencies.

1.3 Ultraviolet Imaging

UV imaging is generally categorized as near (NUV), middle (MUV), far (FUV), or extreme (EUV) ultraviolet. The UV window spans from deep blue at 400 nm (~ 750 THz) to about 10 nm (~ 30,000 THz) which is approaching the more energetic region of x-rays and gamma rays.

UV light is absorbed or scattered by most particulates and aerosols in the atmosphere and; therefore, it is more difficult to travel long distances. However, UV imaging is useful for many short-range applications. Interestingly, UV light with wavelengths less than 280 nm is solar blind which implies the presence of sunlight does not affect the image as it would with other windows in the electromagnetic spectrum.

Deep UV Raman is a method that uses a laser source with a wavelength, $\lambda < 250$ nm, to excite unknown materials for detection and determination of chemical, biological and explosive (CBE) signatures [24]. For many organic and biological materials, using laser sources within the visible to NIR region involves challenges of sample burning, obscuration from background fluorescence, and diminished detection in ambient light conditions. Using an IR source can avoid

the fluorescence background but has a lower excitation energy and introduces thermal noise. This affects the sensitivity of the measurements. Deep UV Raman avoids these challenges because it has a high excitation energy and falls within a fluorescence-free zone which is favorable for detection and interpretation. Complexity in the design and implementation of a suitable UV laser source limits the practicality of performing Deep UV Raman. Nevertheless, a lab instrument was developed to provide a baseline model for a compact, standoff, handheld system. The lab instrument was empirically tested using 248.6-nm NeCu lasers for military-grade and homemade explosive materials. Results show there is potential for the development of a handheld device. The demonstration is observed to have a good correlation between estimated and actual data in Figure 8.

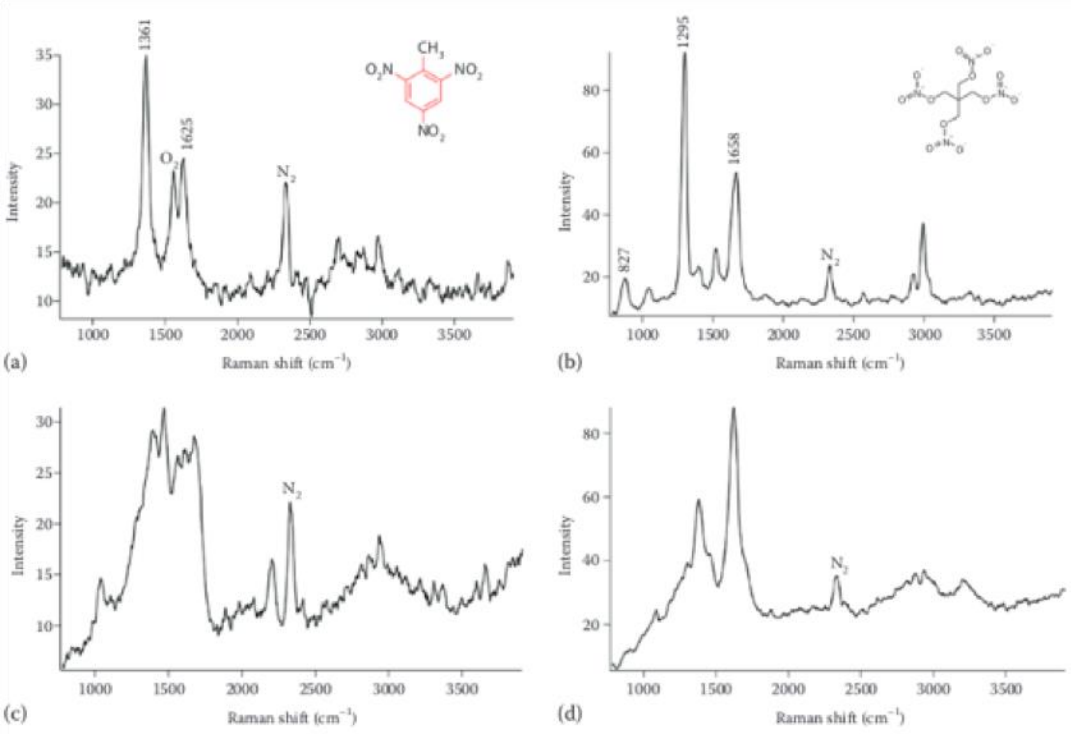

Figure 8: Deep UV Raman spectra of military grade explosives (a) TNT, (b) PETN, (c) C4, (d) Semtex [24].

UV imaging can be used for detecting human traces such as finger prints, urine, semen, hair, and fibers due to their absorptive and luminescent properties [25]. Similarly, materials that absorb near UV light and reflect or emit visible light make them distinguishable from their surroundings as seen in Figure 9. Systems operating at wavelengths in both UV and visible regions provide great contrast and resolution for imaging targets in selective settings.

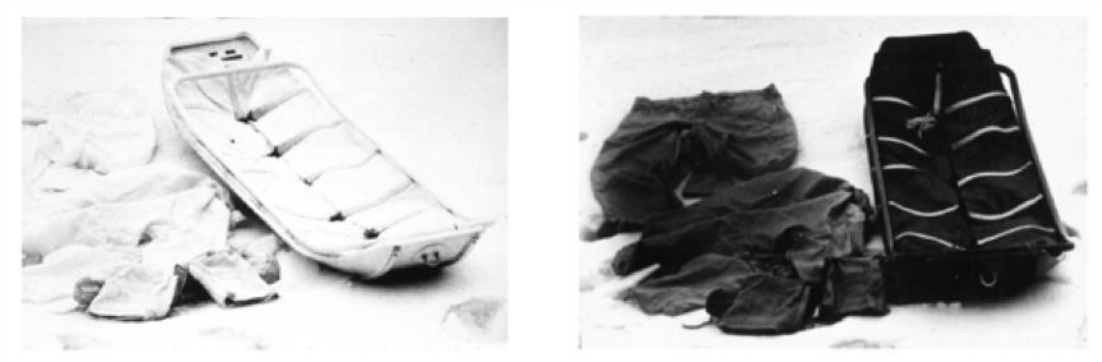

Figure 9: (LEFT) Visible and (RIGHT) Near UV images of Canadian Arctic military gear against snow [25].

Figure 10 illustrates a good comparison of UV, visible, and IR imaging. The distant mountain range is faded in the UV image and clear for all the others. For plants and grass in the sand, the UV and visible images show better contrast than the IR images. The moon is difficult to see in UV and visible images but clear in the IR images. The NIR image clearly shows cloud cover in the distance which no other image provides. In addition, the MIR image provides higher contrast for the facilities in the bottom left and right compared to all other images. Therefore, in this setting, it appears as though UV imaging does not provide any advantage over visible or IR imaging. In fact, in this setting, it appears as though the NIR and MIR images provide all the information needed for the scene.

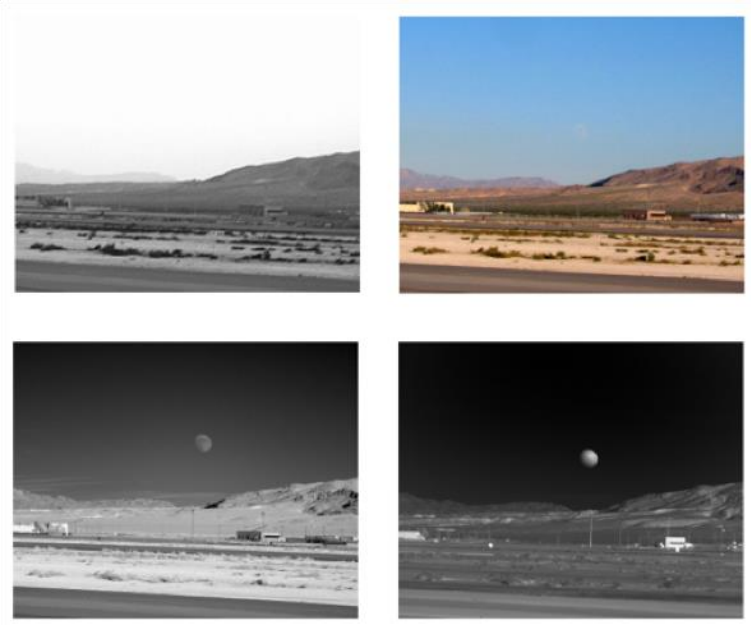

Figure 10: Images in near UV, VIS, NIR, MIR (reading left to right) [25].

In summary, UV imaging is useful for applications that require detecting and identifying specific material properties. While methods are available in the visible to IR regions, Deep UV Raman is the best option for future systems detecting and identifying explosive materials. With advancements in UV laser sources, it will be feasible to design a compact, standoff, handheld system for Deep UV Raman. In addition, UV imaging is useful for recognizing human traces against UV-absorptive backgrounds as well as distinguishing UV-absorptive materials against visible-reflective backgrounds. UV imaging is not advantageous in all settings, but for specific applications; it provides capabilities unattainable using visible, IR, mmWave or lower frequencies.

Chapter 2

Methodology

2.1 Additive Manufacturing

Many techniques for additive manufacturing are available and involve different processes and materials capable of developing optical components. For results provided in this study, the 3D printer used is a FORMLABs stereolithography (SLA) Form 2. Stereolithography uses a laser to cure liquid resin while some other approaches; such as, selective laser sintering (SLS) uses a laser to melt and bind powdered material [26, 27]. Fused deposition modeling (FDM) is also very common and uses a heated nozzle to melt and bind thermoplastic filament. Laser-based 3D printing is a practical approach for optical components because the resolution is typically dependent on the beam width of the laser. While FDM printers may not have the same resolution as laser-based printers, the post-processing methods discussed in this report may be applicable. The methodology may enable the ability to develop optical-quality components from initially low-quality printed substrates. For specific details regarding the processes and capabilities of 3D printers, companies in the additive manufacturing industry provide information on their websites.

2.2 Surface Smoothening

Although the primary focus of this report is on the topic of additive manufacturing, it is important to recognize a few commercial practices that serve as examples of subtractive manufacturing. Fly-cutting, ball-end milling, and non-circular turning are some common methods for diamond machining and are capable of producing freeform optical surfaces by

‘shaving’ off layers to obtain the desired shape [28]. The resulting geometry is accurate and the surface is smooth. However, each method has its limitations in terms of the maximum slopes, radii of curvatures, and size of the optics. In comparison, additive manufacturing allows for extreme slopes and radii of curvatures as well as various sizes of the optics dependent on the type of printer. While 3D printing provides more control over the design and dimensional complexity, it has less control over the surface smoothness. Therefore, post-processing methods such as those discussed in this report enable additive manufacturing the ability to produce optical-quality components.

To fill in grooves on surfaces after 3D printing, an application engineer from FORMLABs explored what is called the dipping method. This is accomplished by immersing a printed substrate in liquid resin to fill cracks, pinholes, and other undesirable defects inherent to the printing process [29]. After the substrate is post-cured with UV light, it adopts a smooth surface finish. This process can be repeated and is shown to work well with resin-based substrates but it may be possible to extend the use for other compatible materials.

Vapor polishing is another method that could fill in grooves for 3D printed surfaces. A common technique for FDM printed substrates is to chemically dissolve the material using liquid acetone. Improving upon this method, a group of individuals vaporized acetone to polish the surface of a thermoplastic called acrylonitrile butadiene styrene (ABS) [30]. Results indicate the surface roughness on a curved fillet is improved from 2950 nm to 35 nm. Other materials were not demonstrated in this study but the concept of using a vapor to polish 3D printable material appears to be quite promising.

Pulse-reverse-current (PRC) electroplating is a smoothing technique that alternates pulses of anodic and cathodic current to laminate valleys and delaminate peaks for metallic surfaces

[31]. PRC continuously replenishes metal ions in the diffusion layer which raises the limiting current density as well as provides greater bath stability and efficiency. In addition, thickness buildup in high current density areas is eliminated due to the current reversal pulses. Therefore, PRC is capable of producing brighter and smoother surfaces than standard pulse or direct current electroplating. Depending on the application, electroplating can be easily modified to enhance morphology and mechanical properties. For the purpose of this report, Nickel (Ni) PRC is utilized because it offers the best surface characteristics for high-resolution applications. Nickel possesses several advantages over other metals such as good material distribution, low internal stress, high hardness, toughness, and corrosion resistance [32].

2.3 Conformal Coating Techniques

The following discusses vapor deposition and electroless plating. Some alternative options are provided to consider tradeoffs that are dependent on the selection of materials as well as printing capabilities. For this experiment, a nonconductive plastic component is 3D printed, then seeded with a metallic layer using vapor deposition, and electroplated using the PRC method.

Common procedures for depositing films onto optical components involve chemical deposition, sputtering, and vacuum evaporation [33]. Reflective coatings consist of either multilayer dielectric stacks, a single metallic coating, or a combination depending on the intended use. Generally, metallic layers provide the largest spectral bandwidth while dielectric stacks provide the highest reflectance. Ion beam and plasma sputtering are both known to produce extremely high-quality optical coatings that can withstand high irradiance of laser

beams. However, for the purpose of this study, electron beam physical vapor deposition (EBPVD) is the primary focus.

The following information provides critical details to perform vapor deposition properly. First and foremost, the substrates need to be cleaned, rinsed, and dried appropriately. After cleaning and prior to coating, exposure to gas discharge may be used to enhance adhesion by bombarding the surface with ions. The metal to be deposited must be chosen such that it is compatible with the substrate material with respect to its hardness, thermal expansion, thermal conductivity, and the degree to which it outgasses in a vacuum. Plastic-based materials generally have a higher thermal expansion and outgas more than most metals which necessitates a slower pump down and heating of the chamber. During deposition, the contour of substrates has an impact on the uniformity of thickness distribution. Since deposition occurs by the 'line of sight,' there could be portions of the substrate that are essentially shadowed which will not be coated. For this experiment, planetary rotation is used which significantly helps the thickness distribution be less sensitive to changes in the substrate and the source. After deposition, the same principles apply regarding cooldown and returning the chamber's pressure back to atmospheric pressure. Although EBPVD could be used for placing the final surface finish, it is performed for this experiment as an intermediate step to obtain a conductive seed layer. Alternative methods could be used to obtain a similar result. For example, 3D printing with available conductive resins, inks, filaments, and powders would most likely be a cheaper and quicker alternative for obtaining a conductive surface for electroplating.

An electroless plating method could be performed to coat Ni, Cu, Au, and Ag on nonconductive plastic substrates but there are some tradeoffs to be considered [34]. The process is driven by a chemical reaction rather than an external electrical current which allows for thicker

coatings to be deposited in less time. Rather than needing to place a conductive seed layer, the substrate is directly dipped in a bath to sensitize the desired surface that will be coated. Then, depending on the method, it will undergo steps like activation, reduction, and acceleration to coat the surface with a metallic layer. Electroless plating conformally coats a surface regardless of the contour which can be quite useful in some applications. Consequently, to produce optical-quality components, this method requires an initial substrate surface that is smooth and without defects. It may be advantageous using electroless plating or alternative methods when the substrate material cannot handle vacuum deposition or other techniques placing a conductive seed layer. However, since the requirements for initial substrate conditions are more stringent, electroless plating reintroduces the challenge of additively manufacturing smooth and unblemished printed substrates. Whereas, current-driven PRC electroplating offers some flexibility for surfaces that may not be smooth or unblemished.

Chapter 3

Experimental Results and Observations

The experimental results will be structured in subsections on grain size, cracks, pinholes, and contamination. Flat and convex mirrors were developed for comparison. Results providing the best argument for the topic of discussion will be presented.

Initial substrates were developed using a stereolithography 3D printer from FORMLABs. After printing, the surface is smoothed with the dipping method and then coated with a metallic, conductive layer using EBPVD. A pulse-reverse-current technique was used to electroplate Ni onto the conductive surface and generate a smoother, more reflective component. Scanning electron microscopy (SEM) and optical profilometry (OP) are used to examine the surface characteristics of the samples which are the primary sources of experimental data.

While there are different approaches, results in this report only focus on vapor deposition and electroplating because, if the combination can be performed with 3D printed components, the options for coating material and respective morphological, mechanical, and radiative properties are extensive. Observations from placing a plastic additively manufactured component in a vacuum chamber can be used to determine whether printed substrates can endure the aggressive environment of vapor deposition. Also, observations from electroplating imperfect surfaces can be used to determine the required intricacy of reaching optical-quality.

3.1 Grain Size

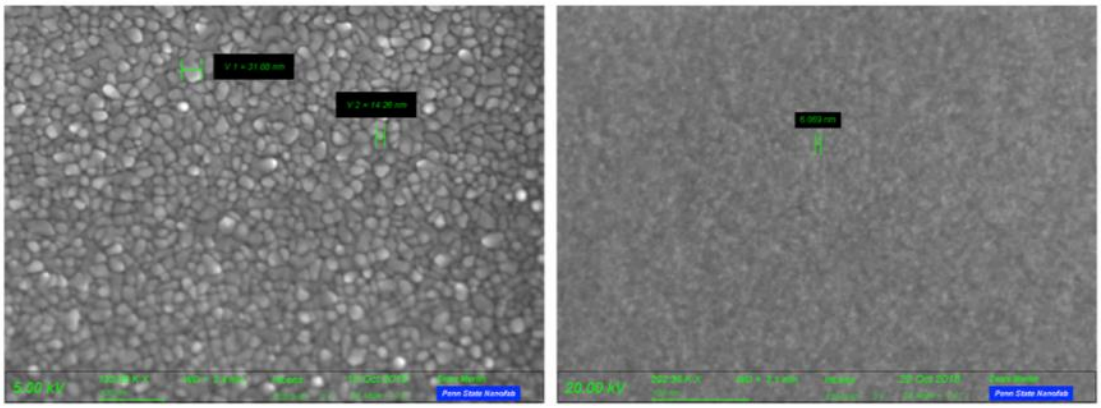

Figure 11: SEM image after EBPVD, before electroplating (LEFT) and after electroplating (RIGHT).

The image to the left in Figure 11 illustrates a grain size less than 40 nm after EBPVD. In other areas of the component, surface defects such as cracks and pinholes were present. PRC electroplating was successful to a remarkable degree as shown in the image to the right which illustrates a grain size less than 10 nm.

3.2 Cracks

Cracks on the surface were observed after EBPVD but post-curing is most likely the cause. After electroplating, the cracks appear to be smoothened by the process which demonstrates there being a degree of freedom for their initial state.

The maximum length of cracks on a flat surface, in Figure 12A, is about 75 microns and on a convex surface, in Figure 12B, is about 200 microns. The curved geometry of a convex surface is observed to affect crack formation. The cracks on a flat surface are thin, short, and dense, whereas, on a convex surface, the cracks are thick, long, but less dense.

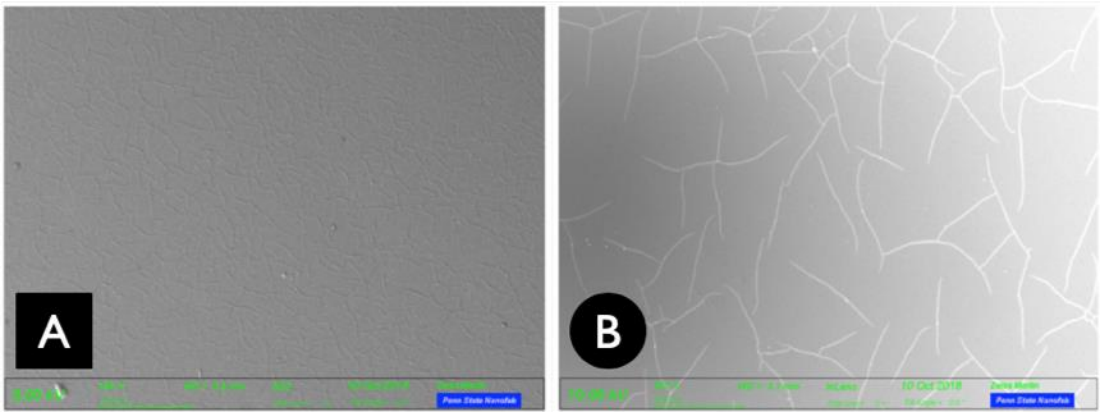

Figure 12: SEM image after EBPVD, before electroplating (LEFT) and after electroplating (RIGHT).

The presence of cracks in Figure 12 suggests a thermal stress had formed during post-curing or EBPVD. However, the reason is most likely due to post-curing which is favorable because post-curing can be adjusted much more easily than EBPVD. The following details provide information supporting the conclusion that EBPVD did not cause the cracks. Acrylic-based plastics generally have a thermal expansion coefficient almost 10 times that of metallic coatings, so it would seem rational to observe a compressive stress during vapor deposition [35]. A compressive stress would form mountain-like structures which is contrary to what the images in Figure 13 indicate. Figure 13C illustrates valley-like cracks nearly perpendicular to one another that do not cross which implies a tensile stress had formed [36]. In addition, Figures 13C and 13D illustrate the valleys are coated with a metallic layer. The depth of the crack in Figure 13B is about 170 nm which resembles the 150-nm coating thickness. This could only mean a tensile stress had caused the cracks prior to deposition. Therefore, the cracks are most likely due to post-curing using high-power UV light over short bursts of time.

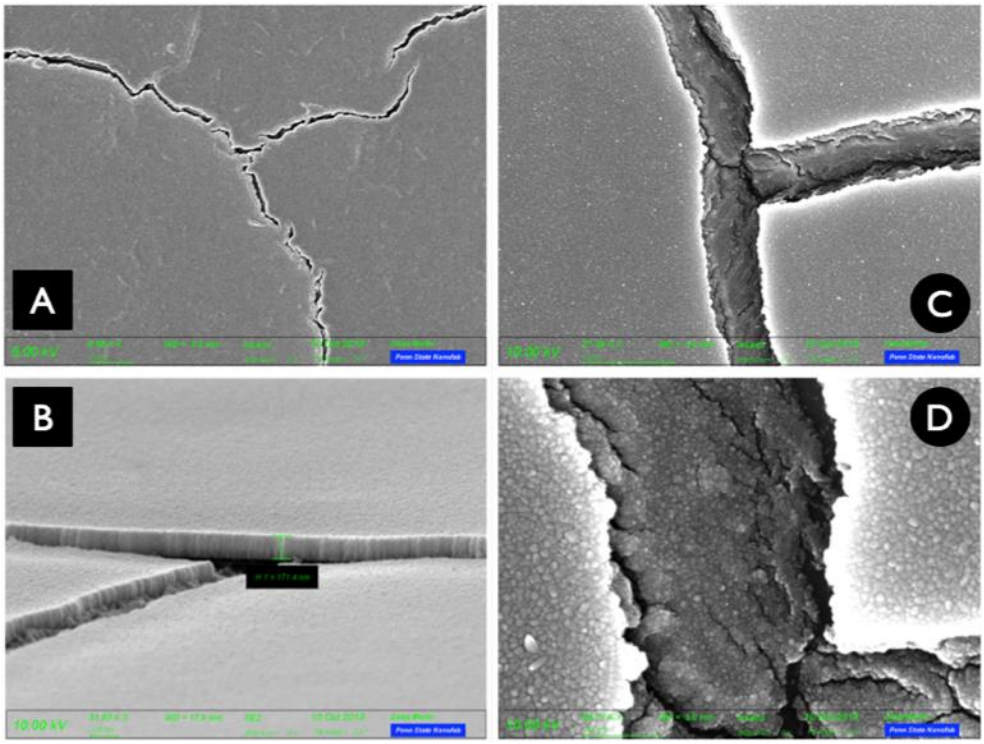

Figure 13: After EBPVD, (A, B) close look at cracks on a flat surface, and (C, D) on a convex surface.

Since the valleys exist prior to EBPVD and they are coated with a metallic layer, a conductive path is maintained within the cracks and throughout the surrounding islands. Therefore, the entire surface can be electroplated in an attempt to seal the cracks, unite the islands, and become a uniformly-coated smooth surface as illustrated in Figure 14A.

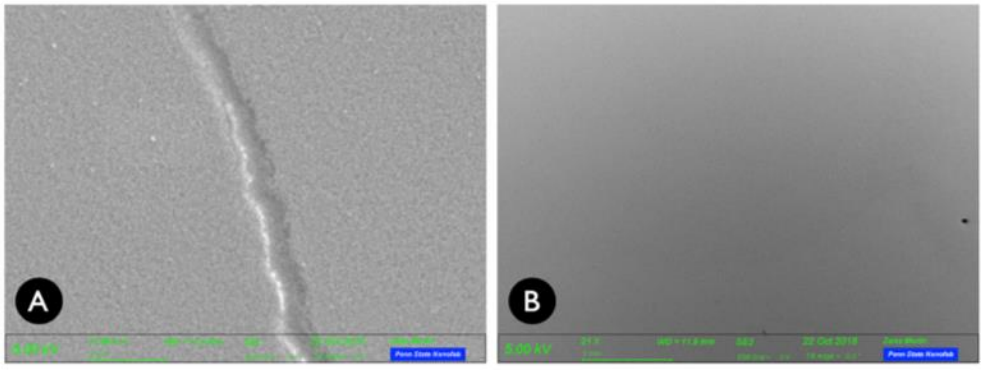

Figure 14: After electroplating, (A) close look and (B) large view of a convex surface.

Figure 14B shows a large view of a convex surface that does not appear to have cracks like in Figure 12B. By comparing Figures 12, 13, and 14, the pulse-reverse-current technique is observed to effectively smoothen the surface. For this experiment, the substrates were electroplated for 30 minutes and produced surprising results. A longer plating time was not tested but it would appear to be a promising remedy for any faded signs of cracks. A leveling agent is mixed into the solution to increase effectiveness and brighten the surface. Also, during the electroplating process, the plating solution is continuously agitated to produce a turbulent flow across the substrate surface.

3.3 Pinholes

Another curious feature is the presence of pinholes that are sporadically dispersed and surprisingly round. They embody sinkhole-like or volcanic-like appearances. They are first observed after EBPVD and then after electroplating. They are not eradicated after electroplating like most cracks, but the interior and surrounding area is observed to be smoother.

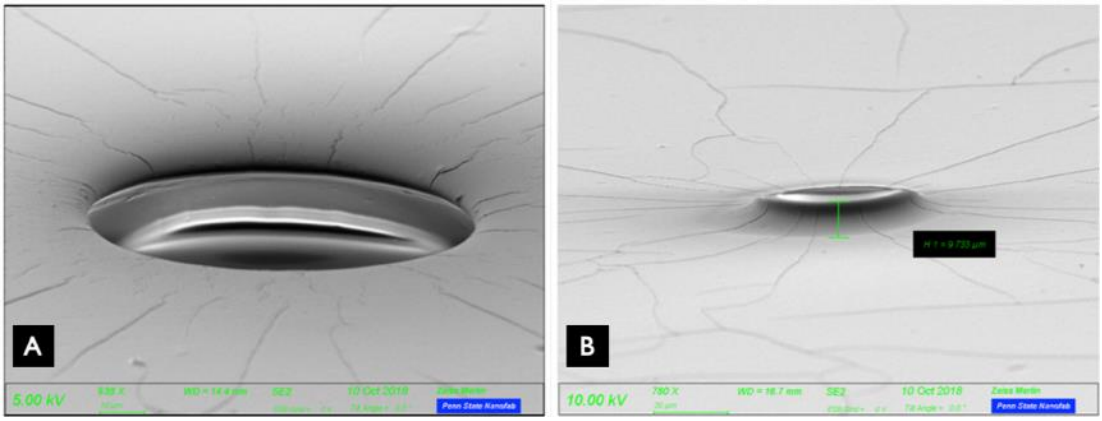

Figure 15: After EBPVD, two shapes are observed: (A) sinkhole-like and (B) volcanic-like.

Details about the pinholes can be extracted from images in Figure 15. The diameter of the pinholes range from about 20 to 100 microns and the height for the volcanic-like pinholes extends to a maximum of 10 microns. It is possible the pinholes are due to outgassing during EBPVD. A chromium layer was directly placed on the plastic without an intermediate lacquer which is supposed to protect the surface from outgassing. The sinkhole-like shapes do not deform the surface like the volcanic-like shapes. Therefore, it is also possible micro-air-bubbles were trapped in the resin before the post-curing process. The cracks originating from the pinholes indicate the air bubbles may have been extracted during the post-curing process. Otherwise, the air bubbles would be extracted while pumping down the vacuum chamber which, in either case, would account for the deformation and the unique roundness of the pinholes.

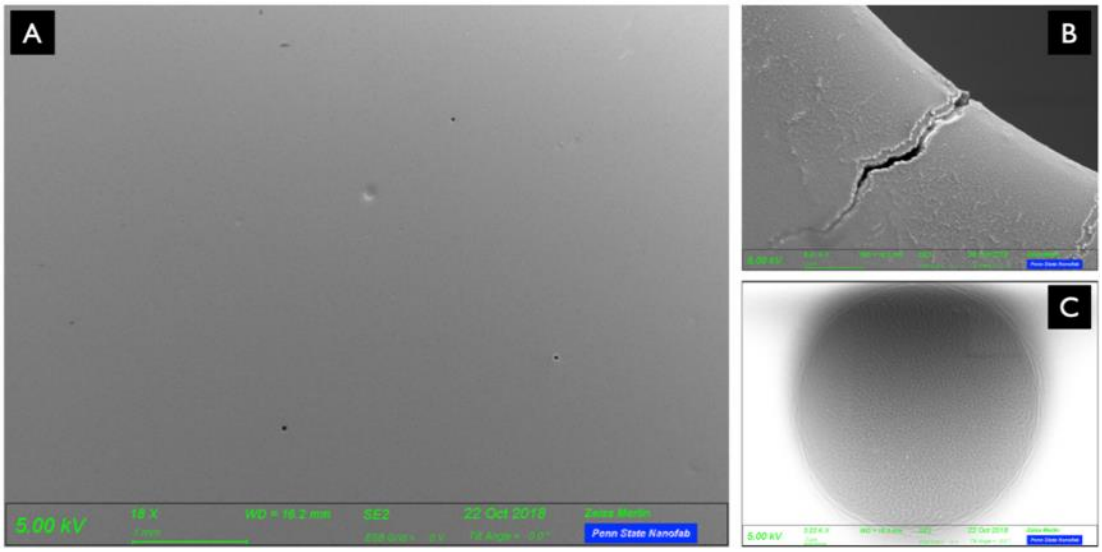

Figure 16: After electroplating, (A) large view, (B) close look, and (C) interior view of pinholes.

Electroplating smoothens the interior region of the pinhole as well as the surrounding area. Figure 16A shows a large view where several pinholes are observed with a few defects but barely any cracks. A closer look at one of the pinholes in Figure 16B shows a crack originating from the pinhole and narrows as it retreats radially. The image illustrates the effect of

electroplating from the crack slowly fading as it narrows and becomes shallower. Since pinholes remain after electroplating, preventive measures must be performed before the post-curing process.

3.4 Contamination

Abnormal surface finishes are observed and believed to be caused by surface contamination. Electroplating is dependent on maintaining a uniform electric potential across the entire surface of a substrate so that a current can be passed through the solution and drive delamination or lamination. Contaminants on the surface creates a nonuniform conductive area which results in surfaces that will not be coated as in Figure 17 or surfaces that appear porous as in Figure 18.

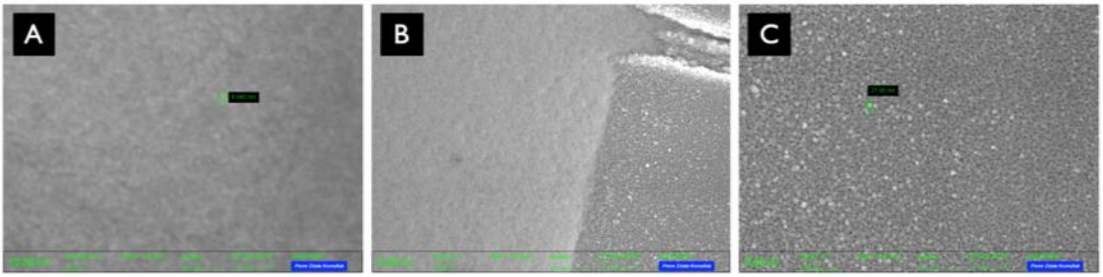

Figure 17: After electroplating, (A) grain size ~ 7 nm, (B) boundary with different grains, (C) grain size ~ 22 nm.

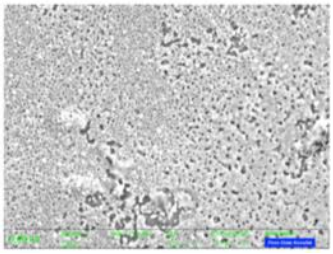

Figure 18: After electroplating, surface appears to be porous.

Chapter 4

Discussion

The following provides information on the novelty of this work with respect to the growing field of additive manufacturing. A 3D printed demonstration for a shared aperture system is proposed with a Cassegrainian configuration. Topics for further research and relevant 3D printing capabilities are also discussed.

4.1 Novelty

The novelty in this work resides in the observations during post-processing. Additively manufactured optics is a developing technology and could serve many applications. But, regardless of the application or its novelty, it is through the methodology to which an application becomes unique or advantageous over the competition.

Detailed observations throughout post-processing reveal hidden, incomplete methodologies that are unexplored. If micro-air-bubbles caused the pinholes, they led to creating perfectly round holes with diameters ranging from 20 to 100 micrometers. The methodology to be explored is intentionally creating micro-air-bubbles and post-curing with varying levels of energy and bursts of time to see the controllability over the depths and diameters. In addition, shallow cracks on a surface are mended by placing a conductive, conformal coating and then PRC electroplating. Pinholes were not mended but they were smoothened. This methodology is unique because it provides a degree of flexibility in the initial quality of additively manufactured components. The methodology to be explored is to quantitatively determine the correlation between the initial quality of components and the plating parameters needed to produce optical-

quality surfaces. Given the right plating parameters, printed parts may be capable of forgoing the post-curing process altogether.

4.2 Demonstration

Figure 19 shows a 3D printed Cassegrain mirror system consisting of a large, concave parabolic mirror (primary) and small, convex hyperbolic mirror (secondary). On the other side of the secondary, where it will not be reflecting rays coming from the primary, there is a small-aperture horn antenna that is designed to operate at 94 GHz. In concept, a 3D printed housing would be used to mount everything together while the waveguide for the antenna would act as a supporting element for the secondary mirror. The printed components were not coated nor tested due to extenuating circumstances. However, this example illustrates how additive manufacturing is capable of printing the components for a combined-aperture system. Several more steps are involved to determine the feasibility of a fully developed system.

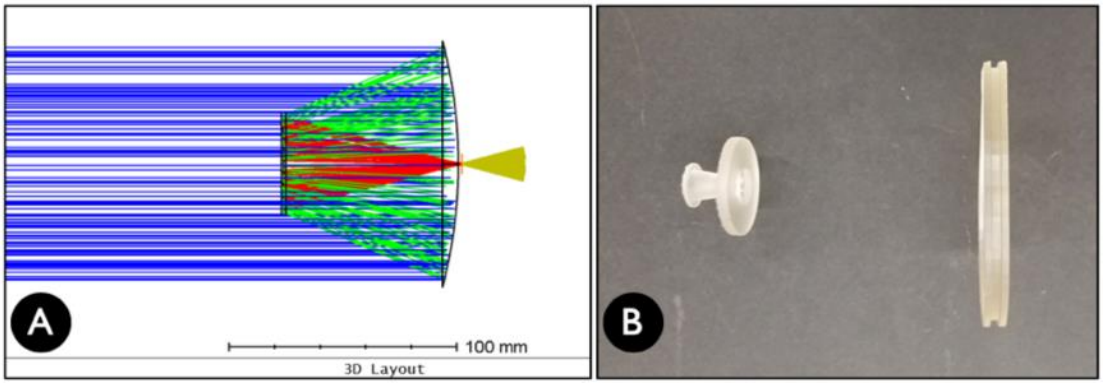

Figure 19: Simulation (A) and 3D printed (B) Cassegrainian configuration.

4.3 Further Development

Further examination of the radius of curvature / flatness, the diameter tolerance, and the modulation transfer function (MTF) would provide a more extensive understanding of how additive manufacturing affects quality and performance. The radius of curvature can be measured using computer generated holography [37] which is capable of testing steep aspheric slopes. Conversely, flatness is commonly tested with optical flats using interferometry. The diameter tolerance can be uniquely measured using shape descriptors to test circularity [38]. This method calculates the deviation of a sample's perimeter from a best-fit circle as a reference. Since a CAD model is typically used for additive manufacturing, this method can be generalized to test the deviation of a sample's contour relative to any shape given a best-fit CAD model as the reference. In addition, by imaging an appropriate test target, the MTF of individual components could determine which type of 3D printed contour fails to meet performance requirements. The MTF can also provide a good measure of system performance as a whole.

The performance of freeform surfaces and gradient-index (GRIN) dielectric lenses are highly dependent on the precision of the 3D printer. Additive manufacturing provides the option to not only print complex geometries but to program specific paths, shapes, or features to be printed in a sequential order. Additive manufacturing simplifies the complexity of fabrication for freeform optical components that are used for foveated imaging systems [39], rearview mirrors [40], or bionic eyes [41]. Freeform surfaces can include shapes with steep slopes, non-symmetric surfaces, and irregular geometries that make fabrication very challenging for subtractive manufacturing. Furthermore, 3D printed GRIN dielectric lenses can be achieved by implementing a space filling curve that uses the ratio of air and printed material to establish an

average dielectric value [42, 43, 44]. For a space filling curve, a FDM printer is programmed to follow a maze-like pattern to allow for air cavities of varying sizes.

Chapter 5

Conclusion

This paper reviews how the mmWave, IR, and UV windows of electromagnetic radiation are utilized with a particular emphasis on military and security applications. While mmWave and IR perform well in various atmospheric settings, UV is capable of identifying chemical, biological and explosive signatures. The methodology was discussed in sections of smoothing and conformal coating techniques. The most prevalent coating technique is pulse-reverse-current electroplating because it is capable of mending cracks and allowing a margin of flexibility for additively manufactured parts. As a result of the observations, the post-curing process may be the cause for most of the defects. However, an interesting process could be explored to intentionally develop periodic pinholes ranging from 20 to 100 microns in diameter. Subsequently, a demonstration was proposed for a shared-aperture Cassegrainian configuration that targets the mmWave, IR, and visible regions. Further research must be performed to provide an extensive quantitative approach for the demonstration and to understand the feasibility of developing 3D printed optical components for multispectral imaging systems. Plastic freeform and aspheric optical components provide a significant advantage over standard optical components for products requiring low weight, complex geometries, or unique performance specifications.

Appendix A

Abbreviations

μm - microns, micrometers

3D - three-dimensional

ABS - acrylonitrile butadiene styrene

Ag - silver

Au - gold

CBE - chemical, biological and explosive

Cu - copper

EBPVD - electron-beam physical vapor deposition

EP - electroplating

EUV - extreme ultraviolet

FDM - fused deposition modeling

FIR - far infrared

FSO - free-space optical

FUV - far ultraviolet

GRIN - gradient index

IR - infrared

LWIR - long wave infrared

mmWave - millimeter wave

MTF - modulation transfer function

MUV - middle ultraviolet

MWIR - midwave infrared

NeCu - neon copper

Ni - nickel

NIR - near infrared

NUV - near ultraviolet

OP - optical profilometry

PRC - pulse-reverse-current

Rh - rhodium

SEM - scanning electron microscopy

SLA - stereolithography

SLS - selective laser sintering

SWIR - short wave infrared

UV - ultraviolet

VIS - visible

BIBLIOGRAPHY

[1] R. Appleby, D. A. Robertson, and D. Wikner, "Millimeter wave imaging: a historical review," Proc. SPIE Conf. on Passive and Active Millimeter-Wave Imaging XX, vol. 10189, May 2017, doi: 10.1117/12.2262476.

[2] L. Yujiri, S. W. Fornaca, B. I. Hauss, R. T. Kuroda, R. Lai, and M. Shoucri, "140-GHz passive millimeter-wave video camera," Proc. SPIE Conf. on Passive Millimeter-Wave Imaging Technology III, vol. 3703, pp. 20–27, Jul. 1999.

[3] L. Yujiri, M. Shoucri, and P. Moffa, "Passive millimeter-wave imaging," IEEE Microwave Magazine, vol. 4, no. 3, pp. 39–50, Sep. 2003.

[4] Y. G. M. Hurtaud, "Millimetre wave propagation over the sea," NATO Technol. Group Rep., Centre d'Electronique de l'Armement (CELAR), Rennes, France, Tech. Rep. AC/243 (Panel 3) TR/3, Oct. 1990.

[5] D. A. Wikner, Millimeter-Wave Propagation Measurement through a Dust Tunnel. U.S. Army Research Laboratory Technical Report ARL-TR-4399, Mar. 2008.

[6] D. A. Wikner, "Passive millimeter-wave imagery of helicopter obstacles in a sand environment," Proc. SPIE Conf. on Passive Millimeter-Wave Imaging Technology IX, vol, 6211, May 2006, doi: 10.1117/12.669170.

[7] N. A. Salmon, "W-band real-time passive millimeter-wave imager for helicopter collision avoidance," Proc. SPIE Conf. on Passive Millimeter-Wave Imaging Technology III, vol. 3703, pp. 28–32, Jul. 1999.

[8] D. A. Wikner, “Millimeter-wave radiometric measurements of a treeline and building for aircraft obstacle avoidance,” Proc. SPIE Conf. on Passive Millimeter-Wave Imaging Technology VI and Radar Sensor Technology VII, vol. 5077, pp. 7–15, Aug. 2003.

[9] N. A. Salmon, R. Appleby, and P. R. Coward, “Polarimetric millimeter-wave imaging,” Proc. SPIE Conf. on Passive Millimeter-Wave Imaging Technology V, vol. 4373, pp. 82–85, Aug. 2001.

[10] F. T. Ulaby, D. G. Long and W. Blackwell, Microwave Radar and Radiometric Remote Sensing. Ann Arbor, MI: University of Michigan Press, 2014.

[11] C. C. Chen, Attenuation of Electromagnetic Radiation by Haze, Fog, Clouds, and Rain, RAND Corporation Report R-1 694-PR, Apr. 1975.

[12] Reference Standard Atmospheres, Document ITU-R P.835-3, International Telecommunications Union Recommendation, 1999.

[13] Attenuation by Atmospheric Gases, Document ITU-R P.676-8, International Telecommunications Union Recommendation, 2009.

[14] Attenuation Due to Clouds and Fog, Document ITU-R P.840-3, International Telecommunications Union Recommendation, 1999.

[15] Specific Attenuation Model for Rain for Use in Prediction Methods, Document ITU-R P.838-2, International Telecommunications Union Recommendation, 2003.

[16] E. Guadagnoli, P. Ventura, G. Barani, and A. Porta, “SWIR range performance prediction for long-range applications,” Infrared Imaging Systems: Design, Analysis, Modeling, and Testing XXV, vol. 9071, May 2014, doi: 10.1117/12.2050282.

[17] A. Arnulf, J. Bricard, E. Curé, and C. Véret, “Transmission by Haze and Fog in the Spectral Region 0.35 to 10 Microns,” Journal of the Optical Society of America, vol. 47, no. 6, pp. 491–498, Jun. 1957.

[18] P. Coward and R. Appleby, “Comparison of passive millimeter-wave and IR imagery in a nautical environment,” Proc. SPIE Conf. on Passive Millimeter-Wave Imaging Technology XII, vol. 7309, Apr. 2009, doi: 10.1117/12.819852.

[19] R. Appleby, P. Coward, and J. N. Sanders-Reed, “Evaluation of a passive millimeter-wave (PMMW) imager for wire detection in degraded visual conditions,” Proc. SPIE Conf. on Passive Millimeter-Wave Imaging Technology XII, vol. 7309, May 2009, doi: 10.1117/12.820827.

[20] W. Yongqing, G. Zongqing, W. Shuonan, and H. Ping, “The temperature measurement technology of infrared thermal imaging and its applications review,” Proc.13th IEEE International Conference on Electronic Measurement & Instruments (ICEMI), pp. 401–406, Oct. 2017.

[21] N. T. Thành, H. Sahli, and D. N. Hào, “Detection and characterization of buried landmines using infrared thermography,” Inverse Problems in Science and Engineering, vol. 19, no. 3, pp. 281–307, Apr. 2011.

[22] N. T. Thanh, H. Sahli, and D. N. Hao, “Infrared Thermography for Buried Landmine Detection: Inverse Problem Setting,” IEEE Transactions on Geoscience and Remote Sensing, vol. 46, no. 12, pp. 3987–4004, Dec. 2008.

[23] M. Al Naboulsi, “Fog attenuation prediction for optical and infrared waves,” Optical Engineering, vol. 43, no. 2, pp. 319–329, Feb. 2004.

[24] P. M. Pellegrino, E. L. Holthoff, and M. E. Farrell, Laser-Based Optical Detection of Explosives. Boca Raton, FL: CRC Press, 2015.

[25] A. A. Richards, Alien Vision: Exploring the Electromagnetic Spectrum with Imaging Technology (Second Edition). Bellingham, WA: SPIE Press, 2011, pp. 1–23.

[26] S. Jasveer and X. Jianbin, "Comparison of different types of 3D printing technologies," International Journal of Scientific and Research Publications (IJSRP), vol. 8, no. 4, pp. 1–9, Apr. 2018.

[27] H. Bikas, P. Stavropoulos, and G. Chryssolouris, "Additive manufacturing methods and modelling approaches: a critical review," International Journal of Advanced Manufacturing Technology, vol. 83, no. 1–4, pp. 389–405, Jul. 2015.

[28] G. Goch, D. Lucca, A. Mehner, H. Prekel, H.-R. Stock, and H.-W. Zoch, "Deposition, machining and measuring of novel hard coatings," in Fabrication of Complex Optical Components (E. Brinksmeier, O. Riemer, and R. Gläbe, (eds.), Springer, Berlin), pp. 133–160, 2013.

[29] FORMLABs, "Guide to transparent 3D printing with clear resin," Tutorials, 9 February 2018, <https://formlabs.com/blog/3d-printing-transparent-parts-techniques-for-finishing-clear-resin/> (2018).

[30] C.-C. Kuo, C.-M. Chen, and S.-X. Chang, "Polishing mechanism for ABS parts fabricated by additive manufacturing," International Journal of Advanced Manufacturing Technology, vol. 91, no. 5–8, pp. 1473–1479, Dec. 2016.

[31] M. S. Chandrasekar and M. Pushpavanam, "Pulse and pulse reverse plating—Conceptual, advantages and applications," Electrochimica Acta, vol. 53, no. 8, pp. 3313–3322, Mar. 2008.

[32] N. G. Sarius, “Surface Technology for Optical and Electrical Connectors,” Ph.D. Thesis, Linköping University, 2010.

[33] P. W. Baumeister, Optical Coating Technology. Bellingham, WA: SPIE Press, Apr. 2004.

[34] B. Viswanathan, “Metallization of plastics by electroless plating,” in Microwave Materials (V. R. K. Murthy, S. Sundaram, B. Viswanathan (eds.), Springer, Berlin), pp. 79–99, 1994.

[35] C. T. Wan, K. A. Taylor, D. L. Chambers, and G. T. Susi, “Metallization of plastics by physical vapor deposition techniques,” in Metallized Plastics 2 (K. L. Mittal (ed.), Springer, Boston), pp. 81–95, 1991.

[36] S. Eroglu and B. Gallois, “Residual stresses in chemically vapor deposited coatings in the Ti-C-N system,” Le Journal de Physique IV, vol. 03, no. C3, pp. C3-155–C3-162, Aug. 1993.

[37] D. Baiocchi and J. H. Burge, “Radius of curvature metrology for segmented mirrors,” Proc. SPIE Conf. on Current Developments in Lens Design and Optical Systems Engineering, vol. 4093, pp. 58–67, Oct. 2000.

[38] K. Misztal and J. Tabor, “Ellipticity and circularity measuring via Kullback–Leibler divergence,” Journal of Mathematical Imaging and Vision, vol. 55, no. 1, pp. 136–150, Dec. 2015.

[39] S. Thiele, K. Arzenbacher, T. Gissibl, H. Giessen, and A. M. Herkommer, “3D-printed eagle eye: Compound microlens system for foveated imaging,” Science Advances, vol. 3, no. 2, p. e1602655, Feb. 2017.

[40] F. Tian, Z. Yin, and S. Li, “Fast tool servo diamond turning of optical freeform surfaces for rear-view mirrors,” International Journal of Advanced Manufacturing Technology, vol. 80, no. 9–12, pp. 1759–1765, Apr. 2015.

[41] K. Pang, F. Fang, L. Song, Y. Zhang, and H. Zhang, “Bionic compound eye for 3D motion detection using an optical freeform surface,” Journal of the Optical Society of America B, vol. 34, no. 5, pp. B28–B35, Feb. 2017.

[42] M. Liang, W.-R. Ng, K. Chang, K. Gbele, M. E. Gehm, and H. Xin, “A 3-D Luneburg lens antenna fabricated by polymer jetting rapid prototyping,” IEEE Transactions on Antennas and Propagation, vol. 62, no. 4, pp. 1799–1807, Apr. 2014.

[43] Z. Larimore, S. Jensen, P. Parsons, B. Good, K. Smith, and M. Mirotznik, “Use of space-filling curves for additive manufacturing of three dimensionally varying graded dielectric structures using fused deposition modeling,” Additive Manufacturing, vol. 15, pp. 48–56, May 2017.

[44] S. Biswas and M. S. Mirotznik, “Customized shaped Luneburg Lens antenna design by additive fabrication,” Proc. 18th International Symposium on Antenna Technology and Applied Electromagnetics (ANTEM), Aug. 2018.

ACADEMIC VITA

Joshua C Davidson

EDUCATION

The Pennsylvania State University – University Park, PA **Graduation: Spring 2019**
Bachelor of Science, Engineering Science & Electrical Engineering
Master of Science, Electrical Engineering
Schreyer Honors College

Relevant Courses: Lasers & Optical Electronics, Electro-Optic Systems and Computing, Micro / Nano Optoelectronic Devices, Optical Engineering Lab, Rf / Microwave Devices

EXPERIENCE

The Pennsylvania State University, College of Engineering – University Park, PA
Spring 2018 - Present
Graduate Research Assistant

- Conduct ITAR Controlled Research on Foveated Imaging and Optical System Design
- Iteratively Design Custom 3D Printed Optics and Assess Performance with Spatial Light Modulation
- Develop Test Procedures & Safety Protocols for Components Operating in Visible, Infrared, & mmWave bands
- Co-authored SPIE Proceedings Paper Considering Foveated Systems on UAV's (doi: 10.1117/12.2305520)

ROCKSAT-XN Grand Challenge Student Rocket – Andøya, Norway
Fall 2017 - Present
Lidar Co-Lead & NASA Laser Custodian

- Designed, Modeled, Assembled, & Installed Lidar Optical System for use on a Sounding Rocket
- In Charge of Class 3b Laser Safety Procedure and Ensuring a Safe Working Environment in Wallops and Andøya
- Verified the Integrated Lidar System meets Design Specifications in a Controlled Environment & In Situ

Texas A&M University, College of Engineering – College Station, TX
Summer 2016
Research Investigator

- Participated in 10 Week Texas A&M - Penn State Research Experience with Hydrogels
- Characterized & Optimized Behavior of pH Sensitive Hydrogels in preparation for Electronics Integration
- Completed Tasks Successfully under $500 Budget and Daily Time Sensitive Constraints

Penn State, College of Engineering – University Park, PA
Summer 2015

Principal Research Investigator

- Performed Independent Research on Antimicrobial Properties of Copper using Different Coating Methods
- Assessed Coating Methods such as Cold Spray, Electroplating, and Electron Beam Physical Vapor Deposition
- Delivered Oral Presentation, Exhibited at Poster Symposium, Documented Results in Research Paper

TECHNICAL SKILLS Competent with MATLAB, SolidWorks, ZEMAX & LabVIEW; Familiar with C/C++, Multisim, Altium, & Verilog

EXTRACURRICULAR

Schreyer Honors College Gateway Orientation
Fall 2017 / 2018

Co-Chair & Assessment Leader

- Generated Ideas & Planned Events for Student Engagement and Networking

Study Abroad in Australia
Spring 2017

Engineering Student

- Studied Engineering at The University of New South Wales in Sydney

Global Engagement Leadership Experience
Fall 2016

Participant

- Participated in Program with 30 Diverse Students to Explore Leadership and Cultural Awareness